MDPI

Article

A Comparative Study of n- and p-Channel FeFETs with Ferroelectric HZO Gate Dielectric

Paul Jacob [1], **Pooja C. Patil** [1], **Shan Deng** [1], **Kai Ni** [1], **Khushwant Sehra** [2,3], **Mridula Gupta** [2], **Manoj Saxena** [4], **David MacMahon** [5] **and Santosh Kurinec** [1,*]

1   Electrical & Microelectronic Engineering, Rochester Institute of Technology, New York, NY 14623, USA; sd2971@rit.edu (S.D.)
2   Department of Electronic Science, University of Delhi South Campus, New Delhi 110021, India; sehrakhushwant@gmail.com (K.S.)
3   Department of Electronics & Communication Engineering, Faculty of Technology, University of Delhi, New Delhi 110007, India
4   Department of Electronics, Deen Dayal Upadhyaya College, University of Delhi, New Delhi 110078, India; msaxena@ieee.org
5   Micron Technology Inc., Manassas, VA 20110, USA
*   Correspondence: skkemc@rit.edu

Abstract: This study investigates the electrical characteristics observed in n-channel and p-channel ferroelectric field effect transistor (FeFET) devices fabricated through a similar process flow with 10 nm of ferroelectric hafnium zirconium oxide (HZO) as the gate dielectric. The n-FeFETs demonstrate a faster complete polarization switching compared to the p-channel counterparts. Detailed and systematic investigations using TCAD simulations reveal the role of fixed charges and interface traps at the HZO-interfacial layer (HZO/IL) interface in modulating the subthreshold characteristics of the devices. A characteristic crossover point observed in the transfer characteristics of n-channel devices is attributed with the temporary switching between ferroelectric-based operation to charge-based operation, caused by the pinning effect due to the presence of different traps. This experimental study helps understand the role of charge trapping effects in switching characteristics of n- and p-channel ferroelectric FETs.

Keywords: ferroelectric; FeFETs; HZO; polarization; charge trapping

1. Introduction

Ferroelectric field effect transistors (FeFETs), particularly hafnium oxide (HfO_2) based FeFETs, have captured the interest of semiconductor technology as the dominant candidates for future memory applications. FeFETs have all the design components of a traditional MOSFET with a sandwiched ferroelectric material layer as the gate dielectric. The two polarization states of the dielectric determine two separate threshold voltages giving rise to a memory window (MW) between two non-volatile memory states.

The discovery of ferroelectricity in hafnium oxide based dielectrics that are CMOS compatible has attracted enormous interests in integrating FeFETs in emerging non volatile memory, in-memory computing, and neuromorphic computing applications [1–3]. Apart from these, FeFETs also find applications in the domain of flexible electronics [4], particularly using structured memory arrays which can be used to mimic important biological functions for brain—inspired computing, or to emulate artificial synaptic responses for neuromorphic computing as discussed above [5]. This is in conjunction with rapid developments in artificial intelligence (AI) technology, which has put forward the requirements for high-speed, energy efficient, and non-volatile memories [6–8]. In this regard, the research community has observed a shift from the existing von Neumann computer architectures,

driven by developments in FeFET technology [9–11]. FeFETs have demonstrated scalability, low power operation due to their CMOS compatibility, and faster non-destructible read/write operation capabilities.

The ferroelectricity observed in ferroelectric materials is primarily due to their non-centrosymmetric structure [1]. A large number of ferroelectric materials have been reported in the literature, however the most popular ones are PZT, PVDF, and HZO [1]. In such materials the polarization direction is controlled by the displacement of the atoms, their degree of variation in crystalline phase and material compositions [12–21].

Among the various dopants in hafnium oxide (HfO_2) such as Al, Sr, La, Gd, Si, and Zr that enable ferroelectricity, Zr doped HfO_2 films have been observed to demonstrate stable ferroelectric behavior over a wide range of temperatures, compositions, and require a lower processing temperature [22–26]. The principle of a FeFET is the change in threshold voltage resulting from the polarization states of the gate dielectric that induce charges at the gate/channel region. Charge trapping remains a major challenge in FeFETs due to the induced threshold voltage (V_{TH}) instability [27]. Hafnium oxide is known to have a high density of intrinsic defects, and the interfaces of HfO_2/interlayer and interlayer/semiconductor are typically defective, which can trap electrons and holes, counteracting the V_{TH} shift induced by polarization switching [28,29]. Figure 1 depicts the effects of up and down polarization in n-FeFET and p-FeFET, comparing with charge trapping effects which are opposite to the polarization effects [28].
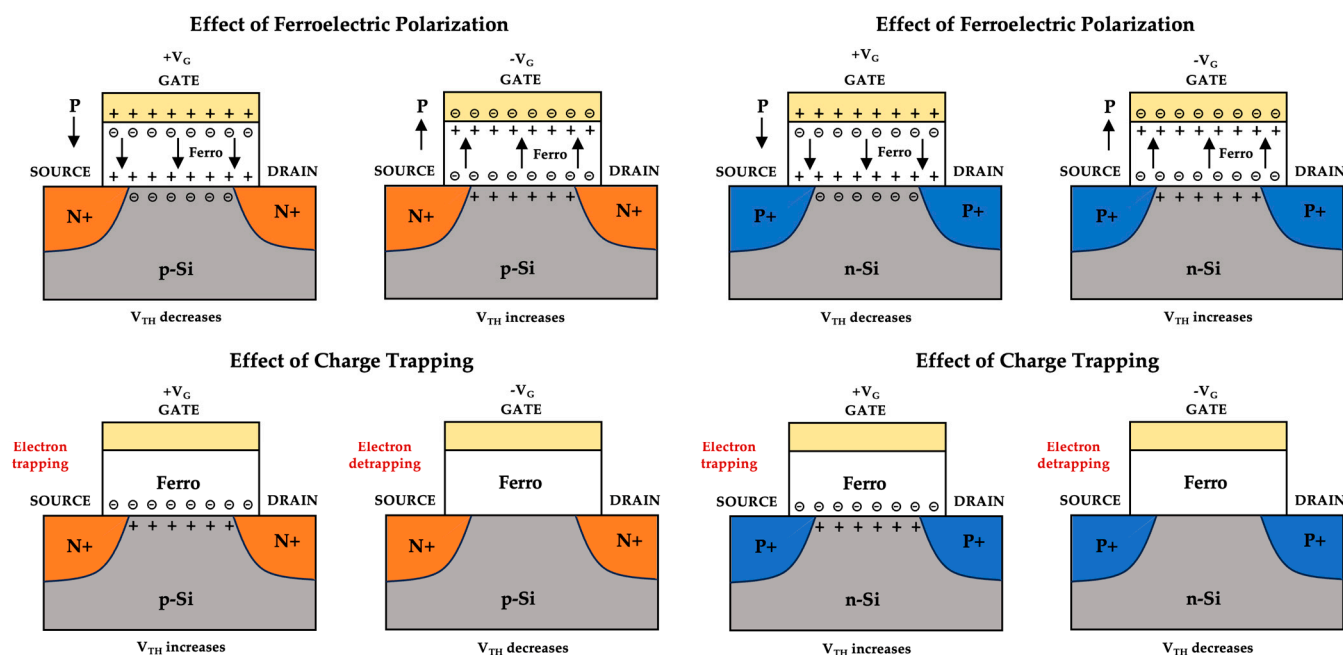
Figure 1. Effect of polarization switching and charge trapping on the threshold voltage shift in MOSFETs.

Hafnium oxide based FeFETs, however, may encounter undesirable charge trapping during the program and erase cycles required for polarization switching [1,22,27]. This is due to the defect density in HfO_2, which limits the span of the memory window post program cycles [1,22,27]. Therefore, the devices demonstrate a slower read operation which leads to a departure from the theoretical values of the memory window (MW) [1,30]. This calls for an early assessment of the different kinds of traps that form in the dielectric stack of the fabricated structure and is the focus of this study.

## 2. Materials and Methods

2.1. Experimental

The FeFETs were fabricated in a student run fab [31] at Rochester Institute of Technology (RIT) on 1–10 Ω-cm base resistivity silicon wafers with 10 nm ALD deposited hafnium

zirconium oxide ($Hf_{0.5}Zr_{0.5}O_2$) as the gate dielectric and 15 nm of sputtered TiN as the gate electrode, followed by an anneal at 600 °C to achieve the ferroelectric phase. The process flow consisted of 5 mask levels designed in-house using Mentor Graphics Pyxis (v10.2), fabricated by a direct laser writer (DWL 66+, Heidelberg Instruments, Heidelberg, Germany) and using an i-line stepper (PAS 5500, ASML, Veldhoven, Netherlands) for lithography. The devices consisted of LOCOS (local oxidation of silicon) isolated FETs with ion implanted source and drain regions implanted by an ion implanter (350D, Varian Semiconductor Equipment, Gloucester, MA, USA). For the n-channel devices, a P31 implant species and p-type substrates were used, and for the p-channel devices a B11 implant species and n-type substrates were used. The process flow and the device schematics are shown in Figure 2, and a detailed process flow for both n- and p-channel devices can be found in Figures S1 and S2 respectively in the Supplementary Materials.
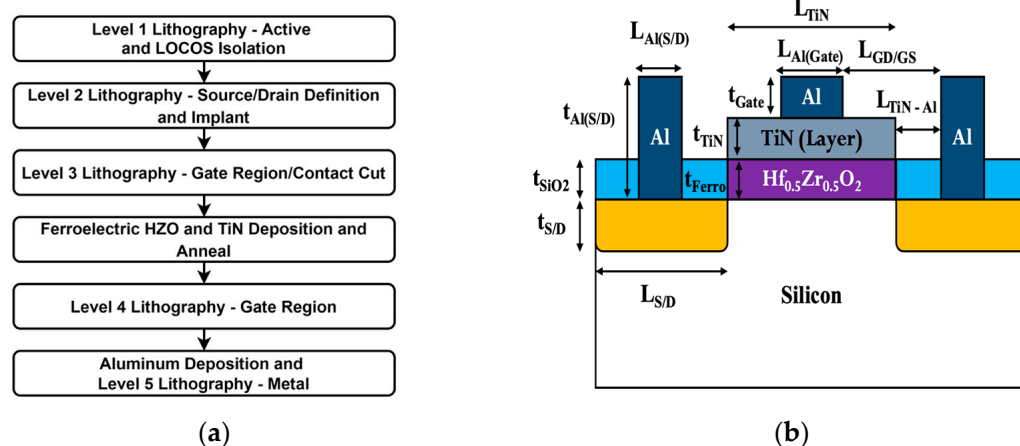
Figure 2. (**a**) Process flow for the fabrication of FeFETs, and (**b**) Schematic diagram of a fabricated FeFET.

A scanning electron micrograph image of a fabricated device (with designed 15 µm channel length and 15 µm channel width) and a high-resolution TEM image of the gate dielectric are shown in Figure 3. A close observation of the TEM image reveals the crystalline nature of the deposited ferroelectric HZO ($Hf_{0.5}Zr_{0.5}O_2$) thin film on the silicon substrate. Further, at the HZO/Si interface, a thin interfacial layer (IL) of SiO_x (~1.63 nm) is observed.
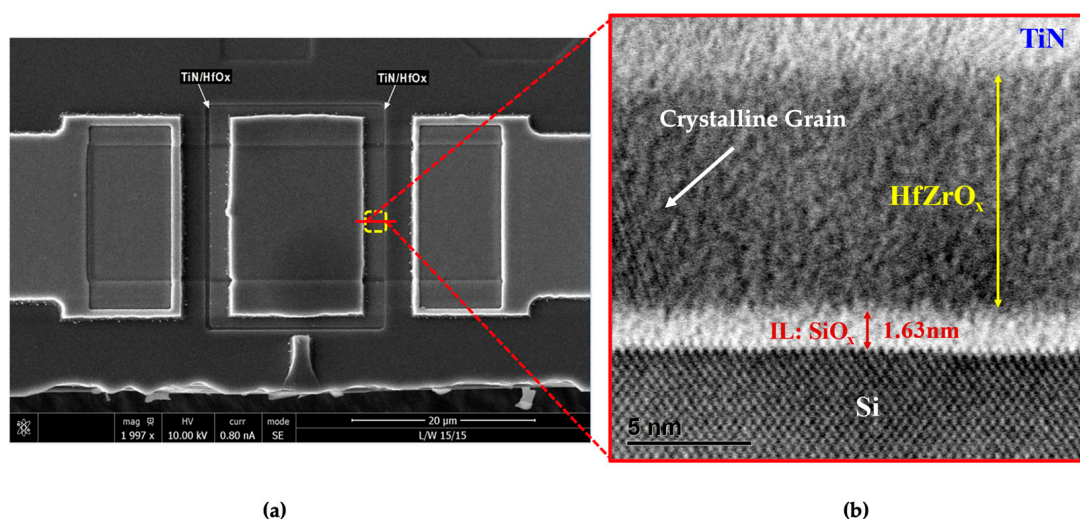

Figure 3. (**a**) SEM image of a FeFET (top view), and (**b**) Cross-sectional TEM image of the gate stack.

2.2. Polarization Characterization of HZO

The HZO layer employed in this work was characterized for its polarization behavior by fabricating MFM capacitors. The fabricated test structure helps in the assessment and characterization of the deposited thin film ferroelectric layers. The layer stack of the MFM capacitor consists of a bottom electrode deposited by sputtering and standard liftoff procedures to realize a 100 nm TiN layer. This is followed by the conformal atomic layer deposition (ALD) of the 10 nm $Hf_{0.5}Zr_{0.5}O_2$ ferroelectric layer. The top electrode, TiN is then deposited by sputtering.

The polarization-electric field (P-E) hysteresis loop of the test structure were recorded with a parameter analyzer (4200-SCS, Keithley Instruments, Solon, OH, USA), illustrated in Figure 4. As observed, the test structure demonstrates good polarization switching behavior with a remnant polarization (P_R) of 17 $\mu C/cm^2$, saturated polarization (P_S) of 27 $\mu C/cm^2$, and a coercive field (E_C) of 1 MV/cm. Also presented is the calibration of a metal-ferroelectric-metal (MFM) capacitor through Silvaco's Victory TCAD (v 1.22.0) simulator, which will be used as a primer for realizing the fabricated FeFETs through TCAD for further analysis [32]. The TCAD modeling of the MFM capacitor relies on the Preisach Ferroelectric model [33], which utilizes the parameters P_R, P_S, and E_C to model the P-E hysteresis loop as shown in Figure 4.
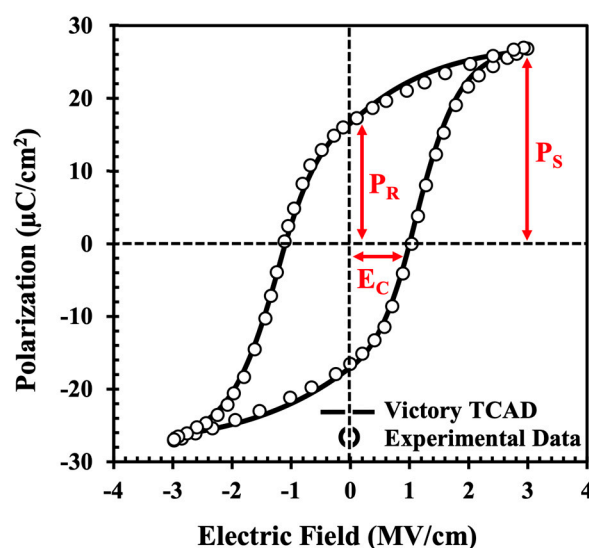
Figure 4. Measured and simulated polarization-electric field hysteresis loop of TiN/10 nm HZO/TiN capacitor.

3. Simulation Methodology

3.1. Experimental Results

3.1.1. DC Characterization

To investigate the DC characteristics, a parametric analyzer (4200-SCS, Keithley Instruments, Solon, OH, USA) was used. The transfer characteristics (I_D vs. V_{GS}) for the n- and p-FeFETs are shown in Figure 5. The memory window (MW) specified at the drain current of 1 nA/μm, and extracted between the high and low V_{TH} states, is observed to be 1 V for the n-FeFET and 1.4 V for the p-FeFET. The DC characteristics of the n- and p-FeFETs demonstrate asymmetric subthreshold characteristics. The p-channel devices exhibit steeper subthreshold characteristics compared to their n-channel counterparts. In addition, the n-FeFETs demonstrate a higher contribution of the gate-induced-drain-leakage (GIDL) current component, suggesting the role of stronger band bending at the accumulation region which is responsible for the setup of high electric fields. This consequently results in the tunneling of the valence band (VB) electrons to the conduction band (CB) while generating holes in the VB, otherwise known as band-to-band tunneling (BTBT). An-

other distinguishing feature of the n-FeFETs is the characteristic crossover point observed during the downward sweep in the transfer characteristics.

(**a**)   (**b**)
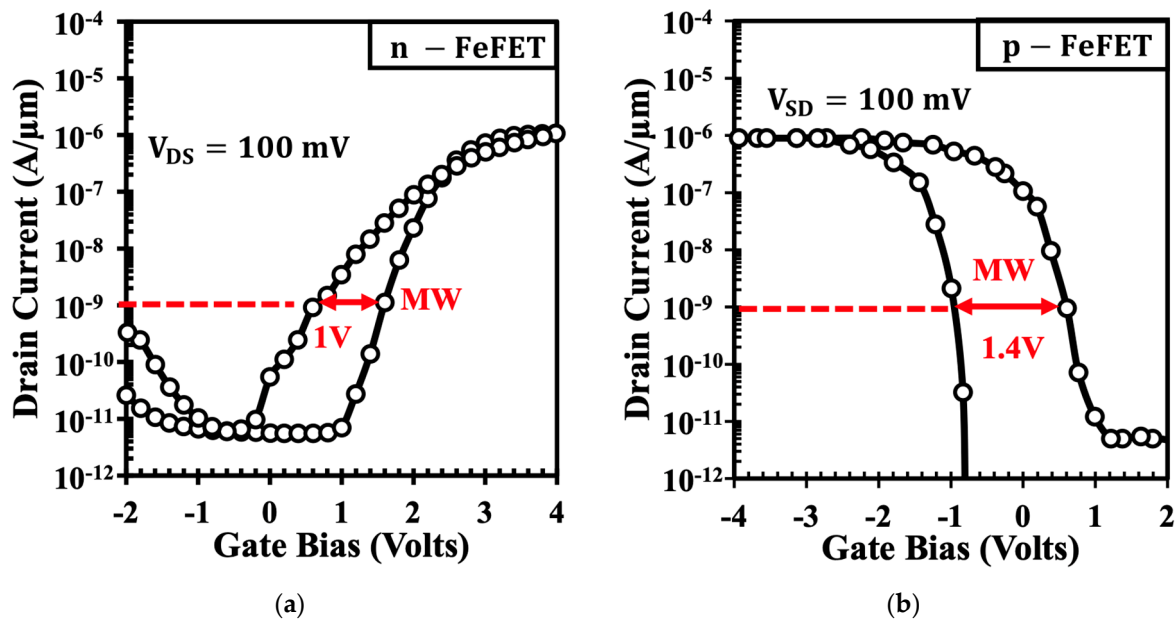
Figure 5. Transfer characteristics of (**a**) n-channel FeFETs, and (**b**) p-channel FeFETs depicting asymmetric behavior.

3.1.2. Pulse Characterization

The fabricated n- and p-channel FeFET devices were characterized through a series of read and write pulse cycles using a probe station (Summit 11000/12000, Cascade Microtech, Beaverton, OR, USA) and a parametric analyzer (4200-SCS, Keithley Instruments, Solon, OH, USA). The pulse setups for the n- and p-channel devices are shown in Figure 6. For the n-channel devices, the height of the reset pulse is set to −4.5 V with a pulse duration of 1 μs, while the set pulse height is varied from 1 V to 3.8 V and the pulse duration is gradually tuned from 50 ns to 0.1 s. The p-channel devices are also subjected to similar pulsing conditions with reversed polarities.

(**a**)   (**b**)
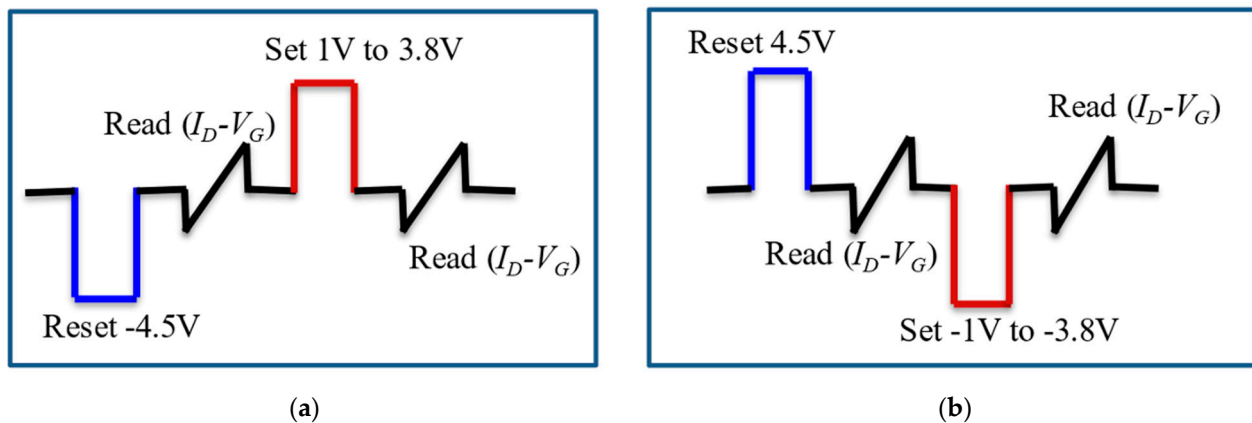
Figure 6. Read and write operations performed at the gate electrode of (**a**) n-FeFET, and (**b**) p-FeFET.

The shift in the threshold voltage (V_{TH}) and the resulting MW for the n- and p-channel devices as a function of pulse width is shown in Figure 7. The switching of the polarization dipoles of a particular ferroelectric layer is a function of both the applied bias and the time duration during which the pulse is applied to the ferroelectric gate stack. As observed

from Figure 7a,c, the V_{TH} of both devices can be tuned gradually by varying both the pulse height and the pulse duration. As the pulse height decreases, a longer pulse is required for observing the necessary switching of the polarization dipoles. For the n-channel FeFETs, a maximum MW of 1 V, is achieved with a pulse height of 3.8 V and pulse duration of 1 μs, as seen in Figure 7b. This point corresponds to the complete switching of the polarization dipoles within the ferroelectric layer. Intermediate pulse height/widths can be utilized for partial polarization in multi-level logic devices. For the p-channel devices, however, the pulse characteristics in Figure 7c,d demonstrate a global maxima in the MW at a pulse duration of 10 μs and a pulse height of −3.8 V. Further, on increasing the pulse width, a characteristic roll-off in the MW is observed as a function of write pulse width.
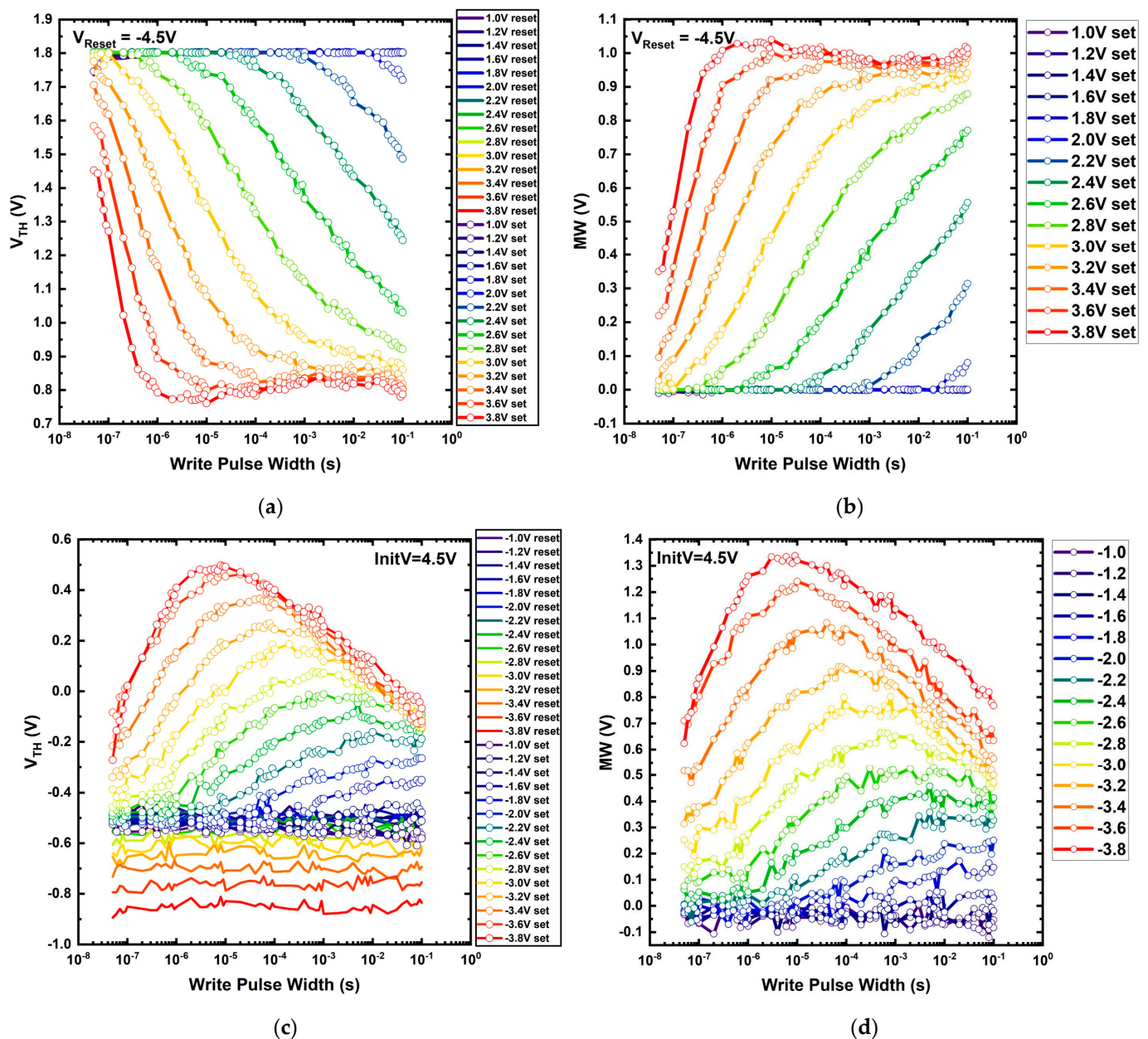
Figure 7. Partial polarization switching by varying the pulse width: (**a**) Gradual tuning of V_{TH}, and (**b**) MW for n-channel, (**c**) Gradual tuning of V_{TH}, and (**d**) MW for p-channel by increasing the width of the program pulse.

The switching behavior investigated using different program/erase pulse heights and widths shows a faster complete polarization switching in n-FeFETs (3.8 V, 1 μs) than in p-FeFETs (−3.8 V, 10 μs).

3.2. Simulation Methodology

The polarization parameters extracted from the test structure's P-E hysteresis loops are fed to the simulation deck to realize ferroelectricity in the HZO. The calibrated simulation deck acts as a primer for realizing FeFET devices for the assessment of the trapping parameters. Table 1 provides the geometrical parameters of the fabricated devices used in simulations.

**Table 1.** Device geometrical parameters depicted in Figure 2b.

Symbols	Description	Value
$N_{D/S}$	Source/Drain Doping	2×10^{19} cm^{-3}
N_{Subs}	Substrate Doping	2×10^{15} cm^{-3}
$t_{S/D}$	Junction depth of Source/Drain	0.8 μm
$L_{S/D}$	Lateral Extensions of Source/Drain	13 μm
t_{SiO2}	Thickness of Silicon Dioxide	100 nm
t_{Ferro}	Thickness of Ferro Layer	10 nm
t_{TiN}	Thickness of TiN Layer	12 nm
t_{Gate}	Thickness of Al Gate Contact	750 nm
$t_{Al(S/D)}$	Thickness of Al Source/Drain Contact	750 nm
$L_{Al(S/D)}$	Length of Al Source/Drain Contact	9 μm

Silvaco's Victory Device simulator is used to identify the different kinds of traps that evolved during the fabrication process [27]. A detailed simulation methodology is presented to capture the switching of the polarization dipoles during the upward and downward sweeps.

Calibration of the Fabricated Devices

In modeling the fabricated devices, p-channel devices are considered first due to their steeper subthreshold characteristics and a parallel memory window. The off-state current is tuned by considering donor type bulk traps in the silicon substrate. The bulk trap density is set as 1×10^{16} cm^3 and the trap level is 0.63 eV. The capture cross section for electrons and holes are set to 10^{-13} cm^2 and 10^{-14} cm^2 respectively in accordance with experimental reports [1,22,34]. Further, the literature survey suggests the role of fixed charges and charge trapping at the HZO/SiO$_2$ interfacial layer (IL) interface in modulating the subthreshold characteristics and thus limiting the memory window of the fabricated devices [1,22,34]. Accordingly, acceptor type interface traps were tuned at the HZO/IL interface to obtain a best fit to the experimental data. In this regard, an interface trap density of 1.8×10^{13} cm^2, trap energy level of 0.20 eV and capture cross sections of 10^{-13} cm^2 and 10^{-14} cm^2 for electrons and holes respectively were defined at the HZO/IL interface [33]. In addition to these, Fermi and SRH models were invoked to capture carrier statistics and the interaction of carriers with traps that evolved during the fabrication process. The Priesach Ferroelectric model was also invoked to model the doping dependent mobility, CVT model [35] and to capture the ferroelectric polarization. The calibrated simulation deck for the p-channel device was then used as the basis for realizing n-channel FeFETs. The off-state current was tuned again by considering the donor type bulk traps in the silicon substrate. The trapping conditions defined in the substrate were similar to that of p-channel devices in order to mimic similar bulk conditions, except that the OFF–state current was tuned by changing the energy of the trap level to 0.43 eV. The interface trap density at the HZO/IL interface was similar to the p-channel case, except that the trap levels were tuned to 0.26 eV to capture the slow subthreshold characteristics observed in Figure 5a for n-FeFETs. In addition to this, to capture the GIDL effect observed in n-FeFETs, as seen in Figure 5a, Kane's BTBT model was invoked, and its coefficients were tuned to achieve the best fit to

the GIDL current [30]. The calibrated simulation decks for the n- and p-channel devices are shown in Figure 8.
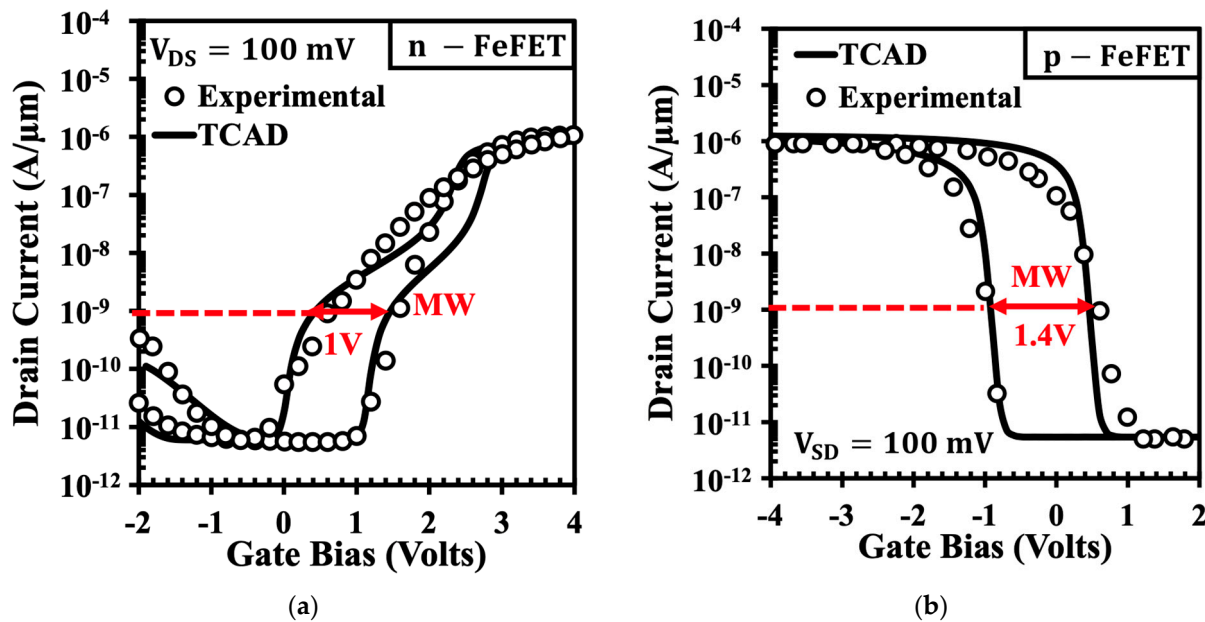
Figure 8. Calibration of simulation deck in Silvaco's Victory TCAD for (**a**) n-channel, and (**b**) p-channel FeFETs.

It is observed that the subthreshold characteristics of n-FeFETs are more affected due to charge trapping at the $HZO/SiO_2(IL)$ interface suggesting that electrons are more easily trapped than holes. This observation essentially stems from the transfer characteristics of the fabricated n- and p-channel FeFET devices. As observed from the subthreshold characteristics of both Figures 5a and 8a, the n-channel FeFET devices demonstrate a gradual change (along with kink) in the subthreshold characteristics, which is a characteristic feature of the trapping and detrapping of the majority carriers, which for the n-channel devices are electrons. On the contrary, for the p-channel devices, as observed from both Figures 5b and 8b, the transfer characteristics, particularly in the subthreshold region demonstrate a steep change with the applied bias without any significant trapping effects as far as the DC characteristics are concerned. From a TCAD perspective, this is achieved by favoring electron trapping by specifying a larger capture cross section area as discussed above and validated from the TCAD simulations shown in Figure 8a. The presence of IL further participates in a tunneling current, due to charge trapping at the HZO/SiO_2 (IL). This results in a charge transfer directly between the HZO and Si channel and is responsible for modulating the subthreshold characteristics of the n-FeFETs [36].

The characteristic crossover point observed in the n-channel devices during the downward sweep was also captured in the TCAD simulations, as shown in Figure 8a. A closer insight into this reveals that there is a temporary switching of the ferroelectric based operation to the charged based operation, which arises due to the presence of the fixed charges and charge trapping at the HZO/IL interface and HZO bulk layer. Under this condition, during the negative sweep, the drain current characteristics are dominated by the carrier trapping which reduces the ON—state current (shown in Figure 8a) as the applied bias is reduced from 4 V to 2 V (denoted as the charge-based operation). The trapped carriers are detrapped as the applied bias is further reduced beyond 2 V, after which, the ferroelectric based operation dominates, giving rise to the memory window (MW) as observed in Figure 8a.

The devices are further investigated by recording the contour plots of electron/hole concentrations and conduction current densities after forward and reverse sweeps at 1 nA/μm. These are depicted in Figure 9a for n-FeFETs and in Figure 9b for p-FeFETs. For

the n-channel device, as observed from Figure 9a, the shift in electron concentration and conduction current density is not significant after the respective program/erase cycles. In contrast, for the p-channel device, a significant change in both the hole concentration as well as the conduction current density is observed in Figure 9b, which accounts for the shift in V_{TH} observed in both Figure 7c,d and Figure 5b after subjecting the gate stack to the necessary program cycle.
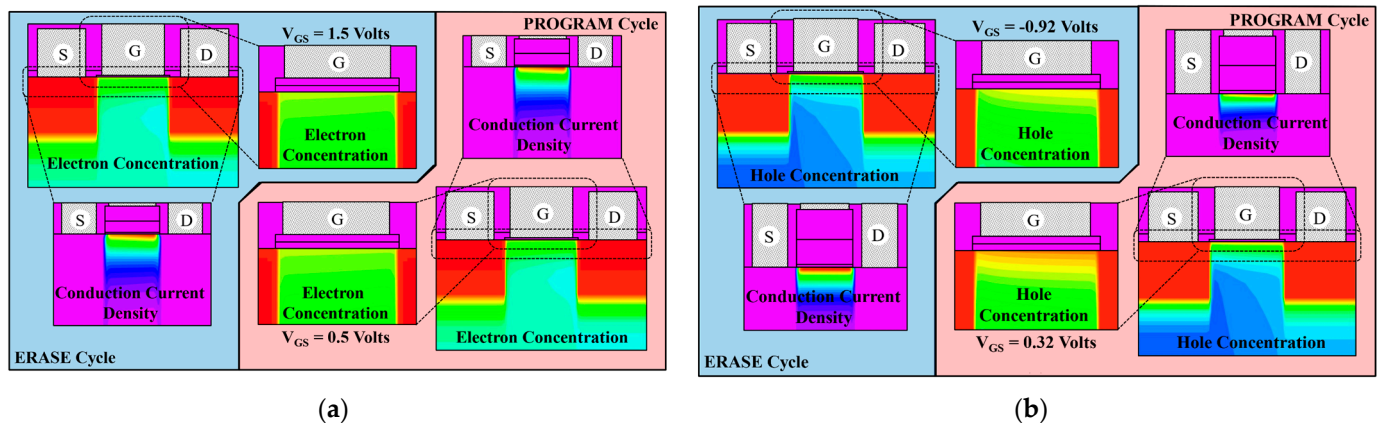
Figure 9. Depiction of electron/hole concentration and conduction current density contour plots for (**a**) n-FeFETs, and (**b**) p-FeFETs.

The trapping effects on the MW can be understood by observing the band diagrams recorded at erase and program conditions. This is shown in Figure 10a,b for the n- and p-channel devices, respectively. For the n-FeFET devices, as depicted in Figure 10a, the carriers can directly tunnel through the HZO and the IL (SiO$_2$) through Fowler-Nordheim (FN) tunneling [37]. The carriers can also participate in tunneling with the help of acceptor type traps defined at the HZO/IL interface and at the HZO bulk through the trap-assisted tunneling (TAT) [37]. The injected carriers are 'hot', in the sense that these carriers are energetic and can further participate in the generation of interface traps at the SiO$_2$ (IL)/Si interface, thereby degrading the quality of the memory window or the devices over time. Consequently, there is a charge sharing directly between the HZO and the silicon channel, which is responsible for modulating the subthreshold characteristics observed in Figures 5a and 8a. Under the program cycle, as depicted in Figure 10b, the electron carriers tunnel through the SiO$_2$ layer, which is translated to the shift observed in the device threshold voltage. Further, on observing the position of the traps with respect to the fermi level under both erase and program conditions, as seen in Figure 10a, it can be inferred that most of the tunneled carriers during the program pulse are trapped courtesy of the bulk traps in HZO and at HZO/IL interface. Consequently, the span of the memory window for the n-FeFETs gets limited.

The band diagrams under erase/program conditions depicted in Figure 10b for p-channel devices follow a similar approach. The tunneling probabilities for the holes, however, is much lower than that of the electrons and the charge sharing through FN/TAT is effectively minimized. At a sufficiently higher gate bias, there is still a possibility of 'hot' hole injection, which may result in the generation of traps at the SiO$_2$/Si interface. Under the program cycle, similar to the n-channel case, the tunneling of the hole carriers through the SiO$_2$ is responsible for the shift in the device threshold voltage observed in Figures 5b and 8b. Further, it is also identified that there are multi-level traps present at the HZO/IL interface. These traps are relatively deeper, as discussed in Section 3.1.1, and are responsible for the roll-off in the device V_{TH} observed during the pulse characterization of the p-FeFET devices in Figure 7c.
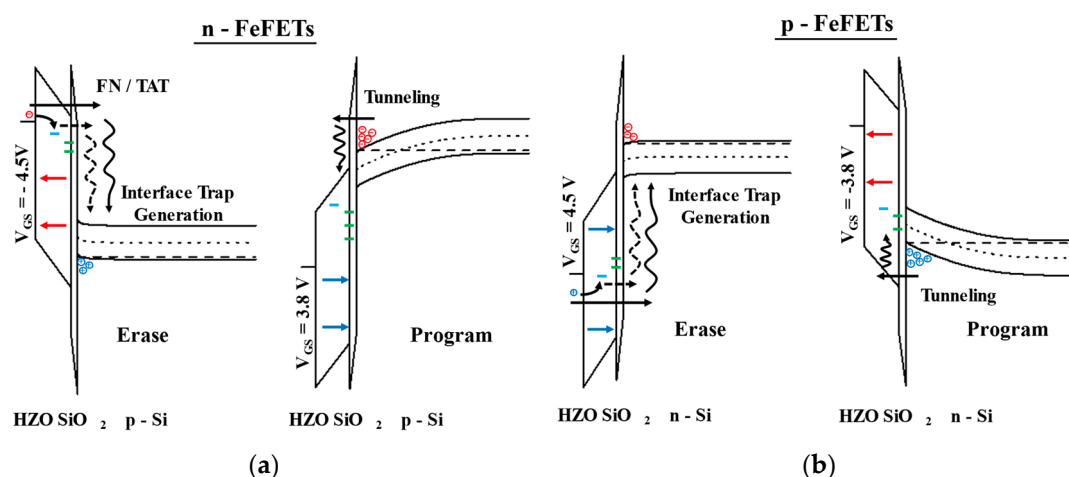
Figure 10. Band diagrams under erase and program conditions for (**a**) n-FeFETs, and (**b**) p-FeFETs. Red and Blue Arrows ($\rightarrow/\rightarrow$) in the SiO_2 dictate the orientation of the polarization field, the Black Arrow ($\rightarrow$) dictates the tunneling direction, while the green and blue symbols (-/-) represent the traps in bulk HZO and HZO/IL interface.

4. Discussion

In this work, n-FeFETs and p-FeFET devices have been designed, fabricated and investigated using a similar process flow, which is important for their integration in CMOS circuitry. A systematic and calibrated TCAD study is presented to investigate trapping effects on the asymmetric behavior observed in the transfer and pulse characteristics of n- and p-channel FeFET devices. For model validation, fabricated MFM capacitors are realized, and the P-E hysteresis loops are calibrated against the experimental set. The calibrated deck is then used to model the FeFETs to identify the trapping parameters. The n-FeFETs demonstrate faster complete polarization switching compared to their p-channel counterparts. It has been observed that the fixed charges and interface traps at HZO/IL modulate the subthreshold characteristics of the fabricated FeFETs and are responsible for the asymmetricity observed in the transfer characteristics of the two devices. Further, the IL facilitates the tunneling current due to the presence of traps in the bulk HZO and at HZO/IL. This is responsible for the charge sharing directly between the HZO and the silicon channel and limits the span of the memory window for the fabricated devices. The n-channel devices, as observed, are identified to be more affected compared to p-channel devices, suggesting that electrons are more easily trapped than holes. Further, the characteristic crossover point observed in n-FeFETs was found to be associated with the partial recovery of the polarization dipoles due to the charge trapping mechanism, which results in a temporary switch between ferroelectric based operation to charge based operation.

Author Contributions: Conceptualization, S.K.; methodology, S.K., P.J. and P.C.P.; software, M.S., K.S. and M.G.; validation, D.M., K.N. and S.D.; formal analysis, P.J., K.S., K.N. and S.D.; investigation, P.J., K.N. and S.K.; resources, S.K. and K.N.; data curation, P.J. and S.K.; writing—original draft preparation, K.S., P.J. and S.K.; writing—review and editing, P.J. and S.K.; visualization, K.N., D.M. and S.D.; supervision, S.K.; project administration, S.K.; funding acquisition, S.K. All authors have read and agreed to the published version of the manuscript.

References

1. Kim, J.Y.; Choi, M.-J.; Jang, H.W. Ferroelectric Field Effect Transistors: Progress and Perspective. *APL Mater.* **2021**, *9*, 021102. [CrossRef]
2. Mulaosmanovic, H.; Ocker, J.; Müller, S.; Noack, M.; Müller, J.; Polakowski, P.; Mikolajick, T.; Slesazeck, S. Novel Ferroelectric FET Based Synapse for Neuromorphic Systems. In Proceedings of the 2017 Symposium on VLSI Technology, Kyoto, Japan, 5–8 June 2017; IEEE: Piscataway, NJ, USA, 2017; pp. T176–T177.
3. Mulaosmanovic, H.; Chicca, E.; Bertele, M.; Mikolajick, T.; Slesazeck, S. Mimicking Biological Neurons with a Nanoscale Ferroelectric Transistor. *Nanoscale* **2018**, *10*, 21755–21763. [CrossRef]
4. Ni, Y.; Wang, Y.; Xu, W. Recent Process of Flexible Transistor-structured Memory. *Small* **2021**, *17*, 1905332. [CrossRef] [PubMed]
5. Han, S.-T.; Zhou, Y. *Photo-Electroactive Non-Volatile Memories for Data Storage and Neuromorphic Computing*; Woodhead Publishing: Cambridge, UK, 2020; ISBN 0128226064.
6. Yoon, S.-K.; Youn, Y.-S.; Kim, J.-G.; Kim, S.-D. Design of DRAM-NAND Flash Hybrid Main Memory and Q-Learning-Based Prefetching Method. *J. Supercomput.* **2018**, *74*, 5293–5313. [CrossRef]
7. Mogul, J.C.; Argollo, E.; Shah, M.A.; Faraboschi, P. Operating System Support for NVM+ DRAM Hybrid Main Memory. In Proceedings of the HotOS, Monte Verità, Switzerland, 18–20 May 2009; Volume 9, p. 14.
8. Ali, T.; Mertens, K.; Kühnel, K.; Rudolph, M.; Oehler, S.; Lehninger, D.; Müller, F.; Revello, R.; Hoffmann, R.; Zimmermann, K. A FeFET with a Novel MFMFIS Gate Stack: Towards Energy-Efficient and Ultrafast NVMs for Neuromorphic Computing. *Nanotechnology* **2021**, *32*, 425201. [CrossRef] [PubMed]
9. Hahnloser, R.H.R.; Sarpeshkar, R.; Mahowald, M.A.; Douglas, R.J.; Seung, H.S. Digital Selection and Analogue Amplification Coexist in a Cortex-Inspired Silicon Circuit. *Nature* **2000**, *405*, 947–951. [CrossRef] [PubMed]
10. Park, Y.; Kim, M.-K.; Lee, J.-S. Emerging Memory Devices for Artificial Synapses. *J. Mater. Chem. C Mater.* **2020**, *8*, 9163–9183. [CrossRef]
11. Merolla, P.A.; Arthur, J.V.; Alvarez-Icaza, R.; Cassidy, A.S.; Sawada, J.; Akopyan, F.; Jackson, B.L.; Imam, N.; Guo, C.; Nakamura, Y. A Million Spiking-Neuron Integrated Circuit with a Scalable Communication Network and Interface. *Science* **2014**, *345*, 668–673. [CrossRef]
12. Isupov, V.A. Phases in the PZT Ceramics. *Ferroelectrics* **2002**, *266*, 91–102. [CrossRef]
13. Chung, C.-C. Microstructural Evolution in Lead Zirconate Titanate (PZT) Piezoelectric Ceramics. Ph.D. Thesis, University of Connecticut, Storrs, CT, USA, 2014.
14. Bhalla, A.S.; Guo, R.; Alberta, E.F. Some Comments on the Morphotropic Phase Boundary and Property Diagrams in Ferroelectric Relaxor Systems. *Mater. Lett.* **2002**, *54*, 264–268. [CrossRef]
15. Zhu, H.; Yamamoto, S.; Matsui, J.; Miyashita, T.; Mitsuishi, M. Resistive Non-Volatile Memories Fabricated with Poly (Vinylidene Fluoride)/Poly (Thiophene) Blend Nanosheets. *RSC Adv.* **2018**, *8*, 7963–7968. [CrossRef] [PubMed]
16. Furukawa, T. Ferroelectric Properties of Vinylidene Fluoride Copolymers. *Phase Transit. Multinatl. J.* **1989**, *18*, 143–211. [CrossRef]
17. Wang, J.; Li, H.; Liu, J.; Duan, Y.; Jiang, S.; Yan, S. On the A→ β Transition of Carbon-Coated Highly Oriented PVDF Ultrathin Film Induced by Melt Recrystallization. *J. Am. Chem. Soc.* **2003**, *125*, 1496–1497. [CrossRef] [PubMed]
18. Lovinger, A.J. Unit Cell of the γ Phase of Poly (Vinylidene Fluoride). *Macromolecules* **1981**, *14*, 322–325. [CrossRef]
19. Kim, S.J.; Mohan, J.; Lee, J.; Lee, J.S.; Lucero, A.T.; Young, C.D.; Colombo, L.; Summerfelt, S.R.; San, T.; Kim, J. Effect of Film Thickness on the Ferroelectric and Dielectric Properties of Low-Temperature (400 °C) $Hf_{0.5}Zr_{0.5}O_2$ Films. *Appl. Phys. Lett.* **2018**, *112*, 172902. [CrossRef]
20. Böscke, T.S.; Müller, J.; Bräuhaus, D.; Schröder, U.; Böttger, U. Ferroelectricity in Hafnium Oxide Thin Films. *Appl. Phys. Lett.* **2011**, *99*, 102903. [CrossRef]
21. Kim, S.J.; Mohan, J.; Summerfelt, S.R.; Kim, J. Ferroelectric $Hf_{0.5}Zr_{0.5}O_2$ Thin Films: A Review of Recent Advances. *JOM* **2019**, *71*, 246–255. [CrossRef]
22. Ni, K.; Sharma, P.; Zhang, J.; Jerry, M.; Smith, J.A.; Tapily, K.; Clark, R.; Mahapatra, S.; Datta, S. Critical Role of Interlayer in $Hf_{0.5}Zr_{0.5}O_2$ Ferroelectric FET Nonvolatile Memory Performance. *IEEE Trans. Electron Devices* **2018**, *65*, 2461–2469. [CrossRef]
23. Park, M.H.; Lee, Y.H.; Kim, H.J.; Kim, Y.J.; Moon, T.; Kim, K.D.; Mueller, J.; Kersch, A.; Schroeder, U.; Mikolajick, T. Ferroelectricity and Antiferroelectricity of Doped Thin HfO_2-based Films. *Adv. Mater.* **2015**, *27*, 1811–1831. [CrossRef]
24. Sharma, P.; Tapily, K.; Saha, A.K.; Zhang, J.; Shaughnessy, A.; Aziz, A.; Snider, G.L.; Gupta, S.; Clark, R.D.; Datta, S. Impact of Total and Partial Dipole Switching on the Switching Slope of Gate-Last Negative Capacitance FETs with Ferroelectric Hafnium Zirconium Oxide Gate Stack. In Proceedings of the 2017 Symposium on VLSI Technology, Kyoto, Japan, 5–8 June 2017; IEEE: Piscataway, NJ, USA, 2017; pp. T154–T155.

25. Lomenzo, P.D.; Jachalke, S.; Stoecker, H.; Mehner, E.; Richter, C.; Mikolajick, T.; Schroeder, U. Universal Curie Constant and Pyroelectricity in Doped Ferroelectric HfO_2 Thin Films. *Nano Energy* **2020**, *74*, 104733. [CrossRef]

26. Anderson, J.D.; Merkel, J.; Macmahon, D.; Kurinec, S.K. Evaluation of Si: HfO_2 Ferroelectric Properties in MFM and MFIS Structures. *IEEE J. Electron Devices Soc.* **2018**, *6*, 525–534. [CrossRef]

27. Yurchuk, E.; Müller, J.; Müller, S.; Paul, J.; Pešić, M.; van Bentum, R.; Schroeder, U.; Mikolajick, T. Charge-Trapping Phenomena in HfO_2-Based FeFET-Type Nonvolatile Memories. *IEEE Trans. Electron Devices* **2016**, *63*, 3501–3507. [CrossRef]

28. Deng, S.; Jiang, Z.; Dutta, S.; Ye, H.; Chakraborty, W.; Kurinec, S.; Datta, S.; Ni, K. Examination of the Interplay between Polarization Switching and Charge Trapping in Ferroelectric FET. In Proceedings of the 2020 IEEE International Electron Devices Meeting (IEDM), San Francisco, CA, USA, 12–18 December 2020; IEEE: Piscataway, NJ, USA, 2020; p. 4.

29. Izmailov, R.A.; Strand, J.W.; Larcher, L.; O'Sullivan, B.J.; Shluger, A.L.; Afanas'ev, V.V. Electron Trapping in Ferroelectric HfO_2. *Phys. Rev. Mater.* **2021**, *5*, 034415. [CrossRef]

30. Lue, H.-T.; Wu, C.-J.; Tseng, T.-Y. Device Modeling of Ferroelectric Memory Field-Effect Transistor (FeMFET). *IEEE Trans. Electron Devices* **2002**, *49*, 1790–1798.

31. RIT Semiconductor & Microsystems Fabrication Laboratory. Available online: https://www.rit.edu/facilities/semiconductor-and-microsystems-fabrication-laboratory (accessed on 30 September 2023).

32. Silvaco Inc., S.C.U. *Victory Device User's Manual*; Silvaco Inc., S.C.U.: Santa Clara, CA, USA, 2015.

33. Kuzum, D.; Park, J.-H.; Krishnamohan, T.; Wong, H.-S.P.; Saraswat, K.C. The Effect of Donor/Acceptor Nature of Interface Traps on Ge MOSFET Characteristics. *IEEE Trans. Electron Devices* **2011**, *58*, 1015–1022. [CrossRef]

34. Bae, H.; Nam, S.G.; Moon, T.; Lee, Y.; Jo, S.; Choe, D.-H.; Kim, S.; Lee, K.-H.; Heo, J. Sub-Ns Polarization Switching in 25 nm FE FinFET toward Post CPU and Spatial-Energetic Mapping of Traps for Enhanced Endurance. In Proceedings of the 2020 IEEE International Electron Devices Meeting (IEDM), San Francisco, CA, USA, 12–18 December 2020; IEEE: Piscataway, NJ, USA, 2020; pp. 31–33.

35. Lombardi, C.; Manzini, S.; Saporito, A.; Vanzi, M. A Physically Based Mobility Model for Numerical Simulation of Nonplanar Devices. *IEEE Trans. Comput.-Aided Des. Integr. Circuits Syst.* **1988**, *7*, 1164–1171. [CrossRef]

36. Mittmann, T.; Materano, M.; Chang, S.-C.; Karpov, I.; Mikolajick, T.; Schroeder, U. Impact of Oxygen Vacancy Content in Ferroelectric HZO Films on the Device Performance. In Proceedings of the 2020 IEEE International Electron Devices Meeting (IEDM), San Francisco, CA, USA, 12–18 December 2020; IEEE: Piscataway, NJ, USA, 2020; pp. 14–18.

37. Khan, A.I.; Keshavarzi, A.; Datta, S. The Future of Ferroelectric Field-Effect Transistor Technology. *Nat. Electron.* **2020**, *3*, 588–597. [CrossRef]